

## Electronic Supplementary Information (ESI) for Soft Matter

### Bacteria-inspired Robotic Propulsion from Bundling of Soft Helical Filaments at Low Reynolds Number

Sangmin Lim, Achyuta Yadunandan and M. Khalid Jawed

\*To whom correspondence should be addressed : M. Khalid Jawed.  
E-mail: khalidjm@seas.ucla.edu

#### This PDF file includes:

Supplementary Methods  
Figs. S1 to S5  
Legend for Movie S1  
SI References

#### Other supplementary materials for this manuscript include the following:

Movie S1

## Supplementary Methods

Full details of physics-based simulation for multi-flagellated soft robot.

### S1. Experiment and design choices.

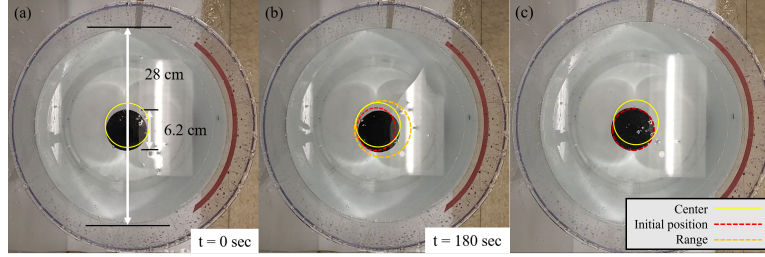


**Fig. S1.** Top view of experiment setting. The robot is placed in the middle. Fig. S1. (a) shows the initial position before the experiment with the dimension of the tank and robot. The yellow solid circle denotes the center of the tank. The red dotted circle in Fig. S1.(b) and (c) shows the robot's initial position. The orange dotted circle shows the maximum range where the experiment started and ended for all our experiments. Fig. S1.(c) shows another experiment trial at  $t = 180$  sec, which is different from Fig. S1.(a) and (b). The position variation between each experiment before and after was similar to the difference between the red circle and the experiment footage shown in Fig. S1.(b) and (c)

**S1.A. Top view of robot inside the glycerine tank.** For the experiment, the robot was placed in the middle to minimize the wall effect. It is known through previous works that the wall boundary can cause a lift toward the wall or to the center of the tank for a rotating cylinder. However, in our experiment, the variation within a single experiment was the variation that can be shown between a red dotted circle and the robot in Fig. S1. (b). Due to the manual placement of the robot, the initial placement varied within the orange dotted circle in Fig. S1. (b). Within this range, the wall effect on the robot was minimal throughout our experiment as could be shown in other experimental case shown in (c).

**S1.B. The geometry choice of artificial flagella and robot body.** Bacterial flagella are known to exhibit polymorphic transformation. Polymorphic transformation can be induced through environmental changes in pH and ionic strength, temperature, reaction towards organic solvents, reaction towards the electric field or mechanical force (1). However, our paper simplifies the problem by investigating pre-formed elastic helical flagella. Current understanding of the polymorphic transformation of bacterial flagella is limited as well as the material that would make it possible requires further investigation to enable more physically appropriate modeling of bacterial behavior. However, our simplification is still within the range of bacterial flagella. Figure S2 displays different flagella geometry of different bacteria strains and polymorphic states in a blue triangle shape with the name and our experimental geometry in a red circle. Our experiment lies reasonably within the geometric range of bacterial flagella in nature. The examples of the species were adapted from Rodenborn et al. (2) Table 1.

Another design concern for the robot was the shape of the head. The actual body of the bacteria is a very flexible ellipsoidal shape. However, the modeling of structure and experimental realization for the cell body of flagellated bacteria are limited (3, 4). Our design is relevantly chosen to ensure concentric rotation of the flagella for each motor with minimal leaking from the gap. The concentric rotation of flagella with minimal gap would be complex with the flexible ellipsoidal body. Furthermore, utilizing our current design, even though it may not be soft and ellipsoidal, we were able to capture the counter-rotation of the robot head and the bundling of the flagella. In future works, we can improve our model and the modeling methods to gain an advantage using the shape of the cell body as well as the flagella interaction (5).

**S2. Elastic Strains, Forces and Jacobians.** In order to understand the Discrete Elastic Rod algorithm (DER), it is essential to understand the elastic strains, associated energy, gradient and hessian of the energy term. As described in the main text, there are three major elastic strains that a Kirchoff rod-based formulation take into account : bending, twisting, and stretching. Bending and twisting strains are node-based quantities while stretching strain is an edge-based quantity. Bending is computed using the curvature binormal vector at each node:

$$(\kappa \mathbf{b})_k = \frac{2\mathbf{t}^{k-1} \times \mathbf{t}^k}{1 + \mathbf{t}^{k-1} \cdot \mathbf{t}^k} \quad [1]$$

The magnitude of this vector is  $2 \tan(\phi_k/2)$  where  $\phi_k$  is the turning angle shown in Figure 4. The curvature vector (i.e. bending strain) at the  $k$ -th node is then

$$\kappa_k = \left( (\kappa \mathbf{b})_k \cdot \mathbf{d}_2^k, -(\kappa \mathbf{b})_k \cdot \mathbf{d}_1^k \right). \quad [2]$$

The twist at each node is

$$\tau_k = \theta^k - \theta^{k-1} + m_{k,\text{ref}}, \quad [3]$$

where  $m_{k,\text{ref}}$  represents the reference twist (i.e. twist associated with the reference frame) and can be calculated from the reference frames (6). In order to account for the rotation of the motor, we included a "natural" twist angle,  $\tau_{\text{motor}} = \omega_T \cdot t$

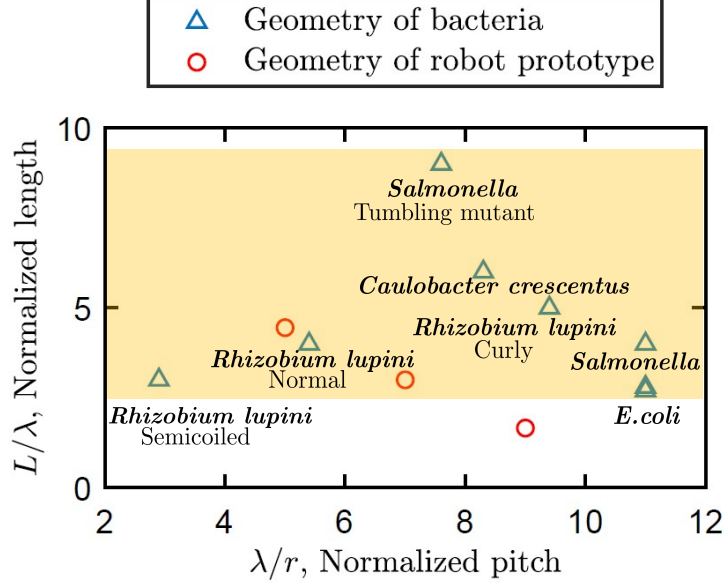


**Fig. S2.** Comparison of existing bacterial flagella geometry and the artificial flagella geometry of the robot prototype. The shaded area shows the range of the bacterial flagella geometry.

(where  $t$  represents time), to the expression for twist at the two nodes representing the motors ( $\mathbf{x}_{m1}$ , and  $\mathbf{x}_{m2}$ ) shown in Figure 4. Then the new equation for integrated twist at  $\mathbf{x}_{m1}$  and  $\mathbf{x}_{m2}$  becomes

$$\tau_k = \theta^k - \theta^{k-1} + m_{k,\text{ref}} - \tau_{\text{motor}}, \quad [4]$$

where  $\tau_{\text{motor}}$  is zero everywhere except at  $m1$  and  $m2$ . Axial stretching ( $\epsilon^k$ ) is an edge-based quantity, which can be represented as

$$\epsilon^k = \frac{|\mathbf{x}_{k+1} - \mathbf{x}_k|}{|\mathbf{e}^k|} - 1, \quad [5]$$

where  $|\mathbf{e}^k|$  denotes undeformed magnitude of the  $k$ -th edge. The energy term associated with the elastic strains can be calculated to be

$$E_k^s = \frac{1}{2} EA (\epsilon^k)^2 |\mathbf{e}^k|, \quad [6]$$

$$E_k^b = \frac{1}{2} EI (|\boldsymbol{\kappa}_k - \boldsymbol{\kappa}_k^0|)^2 \frac{1}{\bar{l}_k}, \quad [7]$$

$$E_k^t = \frac{1}{2} GJ \tau_k^2 \frac{1}{\bar{l}_k}, \quad [8]$$

where  $EA = E\pi r_0^2$  is the stretching stiffness,  $EI = E\pi r_0^4/4$  is the bending stiffness,  $GJ = G\pi r_0^4/2$  is the twisting stiffness,  $G = E/(2(1+\nu))$  is the shearing modulus, and  $\bar{l}_k$  is the reference Voronoi length:  $\bar{l}_k = \frac{1}{2} (|\mathbf{e}^{k-1}| + |\mathbf{e}^k|)$ . The gradient of these energy terms with respect to the degree of freedom provides us with the forces associated with the energy that is required for obtaining the equation of motion. To make sure that our iteration is implicit, we can define the Jacobian terms for the components of equations of motion as,

$$\mathbb{J}_{km}^{\text{inertia}} = \frac{m_k}{\Delta t^2} \delta_{km}, \quad [9]$$

$$\mathbb{J}_{km}^{\text{elastic}} = \frac{\partial^2 E_{\text{elastic}}}{\partial \mathbf{q}_k \partial \mathbf{q}_m}, \quad [10]$$

$$\mathbb{J}_{km}^{\text{ext}} = -\frac{\partial J_k^{\text{ext}}}{\partial \mathbf{q}_m}, \quad [11]$$

where  $\delta_{km}$  is the Kronecker delta function ( $\delta_{km} = 1$  if  $k = m$ ; otherwise  $\delta_{km} = 0$ ). The expressions for the Jacobian terms associated with the elastic forces are available in the literature (6).

In order to decide the level of discretization we have conducted a convergence study for  $\bar{\lambda} = 7$  using normalized robot velocity compared to normalized total angular velocity as shown in Figure S3. The simulation data were collected for a total of 1000 seconds of simulation time with 5 rpm increments from 5rpm to 50rpm. As shown in the figure, the velocity converges very fast even with the number of nodes as few as 37. In order not to sacrifice the speed and accuracy of the coupled simulation, we used 59 nodes, ( $|e| = 5e^{-3}$ ). Corresponding number of nodes for other geometric cases are  $\bar{\lambda} = 9 : 55$  nodes,  $\bar{\lambda} = 5 : 69$  nodes.

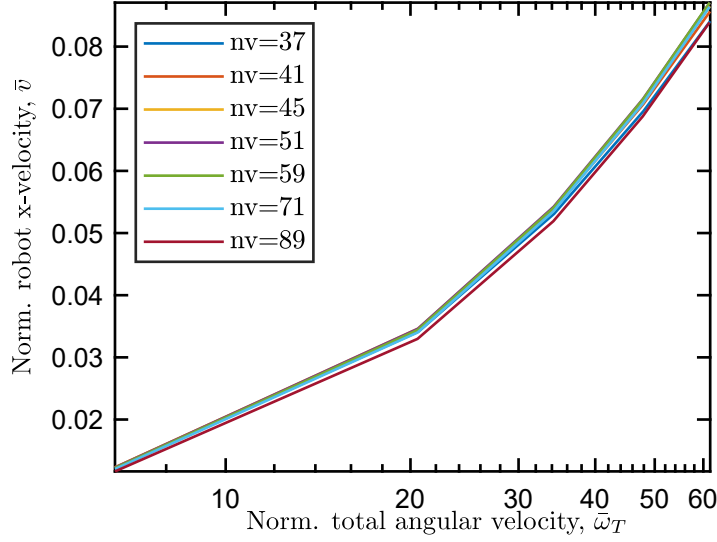


Fig. S3. Convergence study done for  $\bar{\lambda} = 7$ . Nodes numbers of 7 different cases were tested to find an optimal discretization.

**S3. Hydrodynamics model.** We used the Regularized Stokeslet Segments method for the hydrodynamic force on the flagella and Stokes law for the hydrodynamic force on the robot head. Built on the method of regularized Stokeslets, RSS method is beneficial to reduce the sensitivity of the velocity field to the regularization parameter due to its numerical treatment of a weakly singular integral. Cortez presented this method with the assumption that the force field along a filament is piece-wise linear and suggested the possibility of application to piece-wise quadratic or higher degree polynomial (7). Importantly, RSS method accounts for the long range hydrodynamic interaction among flows induced by different nodes on the flagellum. This interaction is ignored by widely used simplified methods, also known as Resistive Force Theory (8).

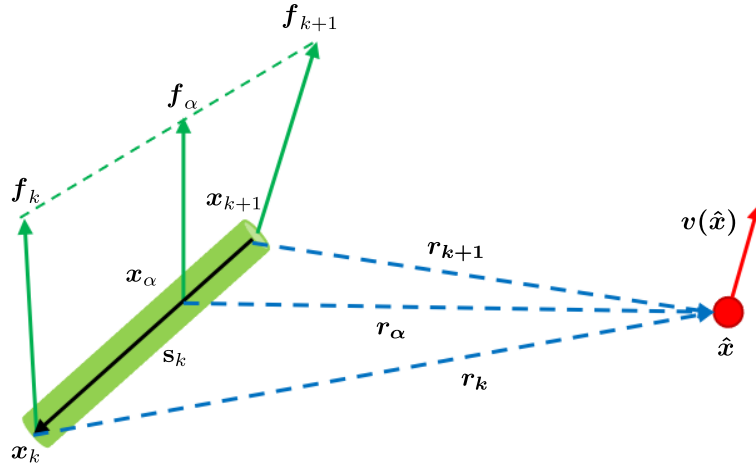


Fig. S4. Notations and discrete schematic of the flow at  $\hat{x}$  generated by a line segment.

Referring to Figure S4, RSS provides a relationship between the velocity at a point ( $v(\hat{x})$  in Figure S4) and the forces applied by each node on the fluid such that

$$8\pi\mu v(\hat{x}) = \sum_{k=0}^{N-2} (M_1^k f_k^h + M_2^k f_{k+1}^h). \quad [12]$$

where  $f_k^h$  is the force vector of size 3 that represents the force applied by the  $k$ -th node onto the fluid. This is equal and opposite to the hydrodynamic force onto the  $k$ -th node. The hydrodynamic force on the  $k$ -th node is the  $4k$ ,  $(4k + 1)$ , and  $(4k + 2)$ -th elements of the hydrodynamic force vector  $f^h$  of size  $(4N - 1)$  in equation 3 in the main text.



The matrices (size  $3 \times 3$ )  $M_1^k$  and  $M_2^k$  are

$$M_2^k = |\mathbf{s}_k| \left( (T_{1,-1}^{k,k+1} + \epsilon^2 T_{1,-3}^{k,k+1}) \mathbb{I} + T_{1,-3}^{k,k+1} (\mathbf{r}_k \mathbf{r}_k^T) + T_{2,-3}^{k,k+1} (\mathbf{r}_k \mathbf{s}_k^T + \mathbf{s}_k \mathbf{r}_k^T) + T_{3,-3}^{k,k+1} (\mathbf{s}_k \mathbf{s}_k^T) \right), \quad [13a]$$

$$M_1^k = |\mathbf{s}_k| \left( (T_{0,-1}^{k,k+1} + \epsilon^2 T_{0,-3}^{k,k+1}) \mathbb{I} + T_{0,-3}^{k,k+1} (\mathbf{r}_k \mathbf{r}_k^T) + T_{1,-3}^{k,k+1} (\mathbf{r}_k \mathbf{s}_k^T + \mathbf{s}_k \mathbf{r}_k^T) + T_{2,-3}^{k,k+1} (\mathbf{s}_k \mathbf{s}_k^T) \right) - M_2^k, \quad [13b]$$

where, as shown in Figure S4,  $\hat{\mathbf{x}}$  is the point of evaluation,  $\epsilon$  is regularization parameter,  $\mathbf{r}_k = \hat{\mathbf{x}} - \mathbf{x}_k$ ,  $\mathbf{s}_k = \mathbf{x}_k - \mathbf{x}_{k+1}$ ,  $\mathbb{I}$  is 3-by-3 identity matrix, and the scalar quantities denoted by  $T$  (e.g.  $T_{1,-1}^{k,k+1}$ ) are described next.

$$T_{0,-1}^{k,k+1} = \frac{1}{|\mathbf{s}_k|} \log \left[ \frac{R + (\mathbf{x}_\alpha \cdot \mathbf{s}_k)}{R} \right] \Big|_0^1, \quad [14a]$$

$$T_{0,-3}^{k,k+1} = - \frac{1}{R \left[ \frac{R + (\mathbf{x}_\alpha \cdot \mathbf{s}_k)}{R} \right]} \Big|_0^1, \quad [14b]$$

$$T_{1,-1}^{k,k+1} = \frac{R}{(|\mathbf{s}_k|)^2} \Big|_0^1 - \frac{(\mathbf{x}_0 \cdot \mathbf{s}_k)}{(|\mathbf{s}_k|)^2} T_{0,-1}^{k,k+1}, \quad [14c]$$

$$T_{1,-3}^{k,k+1} = - \frac{1}{R(|\mathbf{s}_k|)^2} \Big|_0^1 - \frac{(\mathbf{x}_0 \cdot \mathbf{s}_k)}{(|\mathbf{s}_k|)^2} T_{0,-3}^{k,k+1}, \quad [14d]$$

$$T_{2,-3}^{k,k+1} = - \frac{\alpha}{R(|\mathbf{s}_k|)^2} \Big|_0^1 + \frac{1}{(|\mathbf{s}_k|)^2} T_{0,-1}^{k,k+1} - \frac{(\mathbf{x}_0 \cdot \mathbf{s}_k)}{(|\mathbf{s}_k|)^2} T_{1,-3}^{k,k+1}, \quad [14e]$$

$$T_{3,-3}^{k,k+1} = - \frac{\alpha^2}{R(|\mathbf{s}_k|)^2} \Big|_0^1 + \frac{2}{(|\mathbf{s}_k|)^2} T_{1,-1}^{k,k+1} - \frac{(\mathbf{x}_0 \cdot \mathbf{s}_k)}{(|\mathbf{s}_k|)^2} T_{2,-3}^{k,k+1}, \quad [14f]$$

where  $\mathbf{x}_\alpha = \mathbf{x}_k - \alpha \mathbf{s}_k$ , and  $R = \sqrt{|\mathbf{x}_\alpha|^2 + \epsilon^2}$ . Equation 12 can be used to formulate  $3N$  equations (3 per node) that relate the velocities at each node with the forces applied by all the other nodes. Knowing the velocity of each node at the beginning of the time step in DER, this linear system of equations can be solved to obtain the forces and compute the hydrodynamic force vector  $\mathbf{f}^h$ . Since the gradient of the forces with respect to the DOF vector is not available, this force is treated explicitly (Euler forward) in the simulation scheme. Complete details are found in Refs. (7) and (9).

Previously, MRS method prevailed for the analysis in low Reynolds hydrodynamics using Stokeslet methods, however, due to its dependence on the distance between contiguous cutoff functions, the choice of regularization parameter  $\epsilon$  limited the accuracy of calculation. However, RSS method accounts for a continuum of regularized forces therefore decouples the necessity between discretization and the regularization. The regularization parameter used in RSS method  $\epsilon$  for flagella could be interpreted as the radius of the slender filaments. Based on the analysis shown from Cortez (7) we used the regularization value of  $\epsilon = 1.031 \cdot r_0 = 0.00165$  (m).

We now turn to the computation of the hydrodynamic forces on the head ( $\mathbf{f}^{\text{head}}$  in equation 3 in the main text). The middle node along the entire structure ( $\mathbf{x}_h$  in Figure 4) represents the head. As the head is translating (quantified by the velocity of  $\mathbf{x}_h$ ), the viscous medium exerts a drag force onto it. The head is also rotating (quantified by the angular velocity of the head,  $\boldsymbol{\omega}_h$ ) and the viscous fluid applies a torque to resist that rotation. We applied Stokes' law to model the hydrodynamic drag. Since Stokes' law is meant for spherical bodies and the robotic head is cylindrical, we used two numerical prefactors as fitting parameters as discussed next.

The hydrodynamic force on the head ( $\mathbf{x}_h$ ) at time  $t = t_{i+1}$  is

$$\mathbf{f}_h^{\text{head}} = -C_t \cdot 6\pi\mu r_h \left[ \frac{\mathbf{x}_h(t_{i+1}) - \mathbf{x}_h(t_i)}{\Delta t} \right], \quad [15]$$

where  $C_t$  is a numerical prefactor to account for the non-spherical shape of the head,  $r_h$  is the radius of the head (see Table 1), and  $\mathbf{x}_h$  is the position of the head node that can be extracted from the DOF vector,  $\mathbf{q}$ . If the head is the  $h$ -th node in the structure, the vector  $\mathbf{f}_h^{\text{head}}$  of size 3 represents  $(4h-3)$ ,  $(4h-2)$ , and  $(4h-1)$ -th elements of the vector  $\mathbf{f}^{\text{head}}$  in Eq.3. The torque due to rotation of the head is  $\mathbf{T}_h = -C_r \cdot 8\pi\mu r_h^3 \boldsymbol{\omega}_h$ , where  $C_r$  is a numerical prefactor due to the non-spherical shape of the head and  $\boldsymbol{\omega}_h$  is the angular velocity of the head. The angular velocity at  $t = t_{i+1}$  can be computed from the velocities of the two neighboring nodes  $\mathbf{x}_{h-1}$ , and  $\mathbf{x}_{h+1}$  (see Figure 4) such that

$$\omega_h = \frac{1}{|\mathbf{x}_{h+1}(t_{i+1}) - \mathbf{x}_{h-1}(t_{i+1})|^2} |(\mathbf{x}_{h+1}(t_{i+1}) - \mathbf{x}_{h-1}(t_{i+1})) \times [\dot{\mathbf{x}}_{h+1} - \dot{\mathbf{x}}_{h-1}]|, \quad [16]$$

where  $\dot{\mathbf{x}}_{h+1} = \frac{\mathbf{x}_{h+1}(t_{i+1}) - \mathbf{x}_{h+1}(t_i)}{\Delta t}$  is the velocity of the  $(h+1)$ -th node,  $\dot{\mathbf{x}}_{h-1} = \frac{\mathbf{x}_{h-1}(t_{i+1}) - \mathbf{x}_{h-1}(t_i)}{\Delta t}$  is the velocity of the  $(h-1)$ -th node, and  $\times$  represents vector cross product. The hydrodynamic torque is implemented in the simulation as a force-couple, i.e. a force on the node  $\mathbf{x}_{h-1}$  and an equal but opposite force on the node  $\mathbf{x}_{h+1}$ . It turns out that, in case of the specific problem studied in this paper, the magnitude of each force in the force-couple can be approximated to a very good degree as  $\mathbf{T}_h / |\mathbf{x}_{h+1}(t_{i+1}) - \mathbf{x}_{h-1}(t_{i+1})|$  and the angle between two vectors in the right-side of equation 16 is  $90^\circ$ . The direction of the force can be approximated to be equal to  $[\dot{\mathbf{x}}_{h+1} - \dot{\mathbf{x}}_{h-1}]$ . The reason behind these approximations is they result in a simplified expression for the forces and allow us to take the gradient with respect to the DOFs (so that the forces are incorporated into the simulation implicitly). The resulting force on the  $(h+1)$ -th node is

$$\mathbf{f}_{h+1}^{\text{head}} = -C_r \cdot 8\pi\mu \frac{r_h^3}{|\mathbf{x}_{h+1}(t_{i+1}) - \mathbf{x}_{h-1}(t_{i+1})|^2} [\dot{\mathbf{x}}_{h+1} - \dot{\mathbf{x}}_{h-1}]. \quad [17]$$

The force on  $\mathbf{x}_{h-1}$  is

$$\mathbf{f}_{h-1}^{\text{head}} = -\mathbf{f}_{h+1}^{\text{head}}. \quad [18]$$

Equations 15, 17, and 18 are used to calculate the hydrodynamic forces on the head and populate the  $(4N-1)$ -sized  $\mathbf{f}^{\text{head}}$  vector. Note that this vector has only 9 non-zero elements (resulting from the forces on 3 nodes). We fitted the parameters  $C_t$  and  $C_r$  with the experiment velocity along the x-axis which is defined in Figure 5 and head rotation speed for  $\bar{\lambda} = 7$  case. The values for  $C_t$  varied from  $4.9 \sim 5.1$  and  $C_r$  varied from  $0.6 \sim 1.5$  for the simulation sample data. The mean total least squared error from the experimental values were the smallest for the head angular velocity when  $C_r = 0.9$ , and  $C_t = 4.1$  for the x-velocity. We used these values for the head hydrodynamics for analysis of other geometric cases for flagella as well ( $\bar{\lambda} = 5, \bar{\lambda} = 9$ ).

**S4. Contact model.** In this section, the constraint-based contact forces are explained based on the non-penetrative condition between the two edges; we refer the reader to Ref. (10) for complete details. Figure S5 shows two edge segments undergoing collision. We denote the edge segments as  $S_k = (\mathbf{x}_k, \mathbf{x}_{k+1})$  and  $S_m = (\mathbf{x}_m, \mathbf{x}_{m+1})$ , where  $\mathbf{x}_k, \mathbf{x}_{k+1}, \mathbf{x}_m,$  and  $\mathbf{x}_{m+1}$  can be extracted from our DOF vector  $\mathbf{q}$ . In order to formulate a non-penetrative condition, penetration depth ( $\epsilon_{k,m}$ ) is defined as the difference between the minimum Euclidean distance  $\delta_{k,m}^{\text{min}}$  between  $S_m$  and  $S_k$  and sum of the radii of the segment  $S_k$  and  $S_m$ :

$$\epsilon_{k,m} = 2r_0 - \delta_{k,m}^{\text{min}}. \quad [19]$$

In our case, the radius of all the segments are the same and therefore the sum of the radii is always  $2r_0$ .

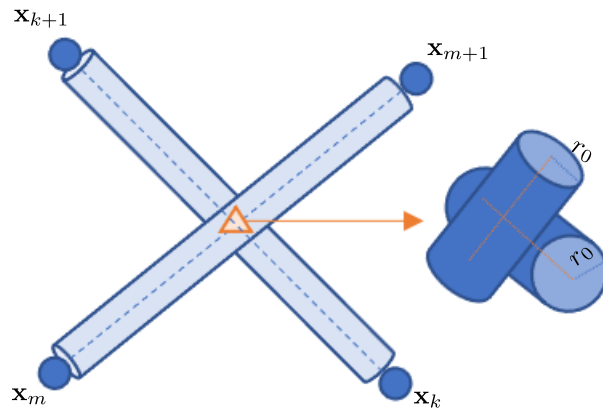


**Fig. S5.** Schematic of contact between two line segments  $S_k$  and  $S_m$ ; orange triangle represents point of contact,  $r_0$  represents the radius of each rod. The minimum distance two segments cannot be smaller than  $2r_0$ .

A contact is detected when  $\epsilon_{k,m} > 0$ . The schematic shown in Figure S5 visualizes the contact condition. After detecting contact, iterations to find interference-free configuration needs to be executed. Using the detected points, the collision

displacements are weighted with the barycentric coordinates of the collision to account for the conservation of mass such that

$$\begin{aligned}\Delta \mathbf{x}_k &= -\frac{1}{2} \mathbf{n}_{km} w_k \\ \Delta \mathbf{x}_{k+1} &= -\frac{1}{2} \mathbf{n}_{km} (1 - w_k) \\ \Delta \mathbf{x}_m &= \frac{1}{2} \mathbf{n}_{km} w_m \\ \Delta \mathbf{x}_{m+1} &= \frac{1}{2} \mathbf{n}_{km} (1 - w_m).\end{aligned}\tag{20}$$

Here, the value of  $\frac{1}{2}$  represents the barycentric ratio of masses with all points having same masses,  $\mathbf{n}_{km}$  represents the minimum distance vector between  $S_k$  and  $S_m$ ,  $w_k$  represents the barycentric coordinate of the contact point on the segment. Iterative process over all the detected contact positions and summing the displacement points for each  $\mathbf{x}_k$ , the displacements with mass conservation could be obtained. We use the penetration depth and compare it with the error tolerance until  $\epsilon_{k,m}^{min} < \text{tolerance}$  for all the detected contact points. The contact force applied at  $k$ -th node due to collision between the contact segments  $S_k$  and  $S_m$  can be evaluated using the  $\Delta \mathbf{x}_k$  values and is represented as

$$\mathbf{f}_k^c = \frac{1}{\Delta t^2} \Delta \mathbf{x}_k m_k,\tag{21}$$

where  $\Delta \mathbf{x}_k$  represents weighted collision displacements with mass conservation consideration,  $\Delta t$  represents the time discretization,  $m_k$  represents the mass of the point (10).

While formulating the DER with contact, we found out that the level of discretization is limited by contact function. Contact method by Spillman and Teschner (10) considers the diameter of the rod so that when two nodes are within the boundary of its diameter, contact could be detected. Therefore, contact limits our length of discretized segment  $|e|$  to be always greater than the diameter of the rod  $2r_0$ .

While the limitation in level of discretization could be a limitation, we used RSS method with our particular choice of the regularization parameter that decouples the viscous force along a line segment from discretization to overcome the limitation. It is shown by Cortez that the level of discretization has insignificant effect on the swimming speed and the trajectory waveform (7).

**Movie S1. Comparison video of multi-flagellated robotic platform and simulation with flagella geometry variation**

## References

1. J Ali, et al., Bacteria-inspired nanorobots with flagellar polymorphic transformations and bundling. *Sci. Reports* **7**, 1–10 (2017).
2. B Rodenborn, CH Chen, HL Swinney, B Liu, HP Zhang, Propulsion of microorganisms by a helical flagellum. *Proc. Natl. Acad. Sci. United States Am.* **110** (2013).
3. H Li, J Tan, M Zhang, Dynamics modeling and analysis of a swimming microrobot for controlled drug delivery. *Autom. Sci. Eng. IEEE Transactions on* **6**, 220 – 227 (2009).
4. JD Martindale, M Jabbarzadeh, HC Fu, Choice of computational method for swimming and pumping with nonslender helical filaments at low reynolds number. *Phys. Fluids* **28**, 021901 (2016).
5. MA Constantino, M Jabbarzadeh, HC Fu, R Bansil, Helical and rod-shaped bacteria swim in helical trajectories with little additional propulsion from helical shape. *Sci. Adv.* **2**, e1601661 (2016).
6. MK Jawed, A Novelia, OM O'Reilly, *A primer on the kinematics of discrete elastic rods*. (Springer), pp. 1–116 (2018).
7. R Cortez, Regularized Stokeslet segments. *J. Comput. Phys.* **375**, 783–796 (2018).
8. BYJ Gray, GJ Hancock, The Propulsion of Sea-Urchin Spermatozoa. *J. Exp. Biol.* **32**, 802–814 (1955).
9. W Huang, MK Jawed, Numerical simulation of bundling of helical elastic rods in a viscous fluid. *Comput. & Fluids* **228**, 105038 (2021).
10. J Spillmann, M Teschner, An adaptive contact model for the robust simulation of knots. *Comput. Graph. Forum* **27**, 497–506 (2008).